Higher-order VLP-based Protein Macromolecular Framework Structures Assembled via Coiled-coil Interactions.

Nathasha D. Hewagama<sup>1</sup>, Masaki Uchida<sup>2</sup>, Yang Wang<sup>1</sup>, Pawel Kraj<sup>1</sup>, Byeongdu Lee<sup>3</sup>, and Trevor Douglas\*<sup>1</sup>

<sup>1</sup>Department of Chemistry, Indiana University, 800 E Kirkwood Ave., Bloomington, IN, 47405, USA

<sup>2</sup>Department of Chemistry and Biochemistry, California State University, Fresno, CA, 93740, USA

<sup>3</sup>X-ray Science Division, Advanced Photon Source, Argonne National Laboratory, Argonne, IL, 60439, USA

#### ABSTRACT

Hierarchical organization is one of the fundamental features observed in biological systems that allows for efficient and effective functioning. Virus-like particles (VLPs) are elegant examples of a hierarchically organized supramolecular structure, where many subunits are self-assembled to generate the functional cage-like architecture. Utilizing VLPs as building blocks to construct twoand three-dimensional (3D) higher-order structures is an emerging research area in developing functional biomimetic materials. VLPs derived from P22 bacteriophage can be repurposed as nanoreactors by encapsulation of enzymes and modular units to build higher-order catalytic materials via several techniques. In this study, we have used coiled-coil peptide interactions to mediate the P22 interparticle assembly into a highly stable, amorphous protein macromolecular framework (PMF) material, where the assembly does not depend on the VLP morphology, a limitation observed in previously reported P22 PMF assemblies. Many encapsulated enzymes lose their optimum functionalities under the harsh conditions that are required for the P22 VLP morphology transitions. Therefore, the coiled-coil based PMF provides a fitting and a versatile platform in constructing functional higher-order catalytic materials compatible with sensitive enzymes. We have characterized the materials properties of the PMF and utilized the disordered PMF to construct a biocatalytic 3D material performing single and multi-step catalysis.

### **KEYWORDS**

Virus-like particles, higher-order assembly, coiled-coils, partitioning, catalysis, nanoreactors.

#### INTRODUCTION

There is a growing interest in the incorporation of biomolecules into materials fabrication. Approaches towards this end have selected biomolecules compatible with the sometimes harsh synthetic conditions.<sup>1, 2</sup> Another approach is to develop materials synthesis approaches that are compatible with the often more fragile biomolecules, like enzymes, to take advantage of the unique and selective chemistry they provide.<sup>3, 4</sup> Incorporation of naturally occurring biocatalysts (enzymes) into materials, for example encapsulation of enzymes inside virus-like particles (VLPs) and their incorporation into higher order materials allows for even greater chemical control, often with added advantages such as increased stability<sup>5,9</sup>, cargo protection<sup>5,9</sup>, enhanced activity<sup>10</sup>, and a means for taking advantage of heterogenous catalysis<sup>11,12</sup>.

Viruses and VLPs are hierarchically organized supramolecular nanostructures, many of which self-assemble from protein macromolecular building block subunits. The structural and functional hierarchy extends from the primary amino acid sequence of well-folded capsid proteins, which self-assemble to form complex viral capsid structures, often in conjunction with viral or non-viral templating molecules. Inspired by natural viral systems, various efforts have been made to build synthetic VLPs tailored for diverse applications by encapsulating and/or displaying a range of cargo/ display molecules inside or outside the capsids, respectively. <sup>13, 14</sup> The modular assembly of capsid proteins, templating molecules, cargo and/or display molecules results in hierarchically complex single VLPs. <sup>15</sup>

The modified VLPs can be exploited as exemplary modular units in constructing two- or three-dimensional (3D) higher-order structures.<sup>13, 16, 17</sup> Various mediator agents are available for building supramolecular VLP assemblies, utilizing different types of interactions between

them.<sup>18</sup> These higher-order composite materials can possess properties beyond those of the individual nanocages, including enhanced stability, altered porosity and surface charge effects, that can be exploited in many synthetic applications.<sup>12, 13, 17-21</sup> Thus, creating 3D structures from VLP cages with desired structural and functional properties is a vibrant research domain.

VLPs derived from bacteriophage P22 are an ideal choice as modular units in fabricating 3D superlattices. Self-assembly of 420 P22 coat proteins (CPs) and 100-300 internal scaffolding proteins (SPs) gives rise to highly symmetric, 56 nm icosahedral VLPs.<sup>22</sup> Foreign cargo proteins can be packaged inside the capsid through a genetic fusion with the SP without compromising capsid assembly,<sup>23-27</sup> to create individual VLP nanoreactors. There are three well-characterized morphologies of P22 with different sizes and porosities: procapsid (PC), expanded (EX), and wiffleball (WB).<sup>28, 29</sup> The EX and WB morphologies are produced by heating the PC form to 65 or 75 °C<sup>28, 29</sup> or treating with sodium dodecyl sulfate (SDS)<sup>30</sup>, conditions where many enzymes lose their activity, making the PC the best morphology for materials design incorporating fragile enzymes.

Negatively charged P22 VLPs can be assembled into arrays using oppositely charged polyamidoamine (PAMAM) dendrimers as linkers using electrostatic interactions and the assembly process has been computationally modeled.<sup>20, 31, 32</sup> The assembly of dendrimer templated arrays is dependent on the ionic strength of the medium, but independent of the capsid morphology or the encapsulated cargo.<sup>11, 12, 32</sup> Modification of the exterior surfaces gives rise to P22 variants with different net surface charges, which has been exploited to gain control over the spatial arrangement of capsids within the assembled 3D structure in the formation of P22-based catalytic superlattices and core-shell VLP architectures.<sup>20, 32</sup>

3D protein framework materials (PMFs) using modified ditopic linkers derived from capsid decoration protein (Dec) can form disordered structures in the absence of a templating molecule like dendrimers. <sup>16</sup> In the presence of dendrimers, P22 assembly can be templated into ordered arrays to which Dec-Dec linkers can be added to lock the particles in place. <sup>11, 12</sup> The Dec-derived linker only binds to the EX or WB P22 morphologies, <sup>11, 12, 16</sup> which requires treating P22 VLPs (PCs) with SDS<sup>30</sup> or heat<sup>28, 29</sup>, compromising the activity of some encapsulated enzymes.

The exterior surface of P22 can be modified to display complementary coiled-coil forming peptide motifs by fusing them with the C-terminus of P22 CP, which is known to extend to the exterior of the assembled VLP in the PC morphology.<sup>33</sup> A coiled-coil protein structural motif is a super helical bundle consisting of two or more  $\alpha$ -helices. They are ubiquitous in nature, and the sequence to structure relationship of coiled-coil motifs has been extensively studied and has facilitated *de novo* material design.<sup>34</sup> The primary sequence of a canonical coiled-coil contains a repeating heptad pattern,  $[a,b,c,d,e,f,g]_n$ , where n is the number of repeats. Positions a and d are typically occupied by hydrophobic residues, forming the hydrophobic core, with the e and g solvent-exposed positions often occupied by charged residues forming ionic interactions, stabilizing the coiled-coil. The self-assembling nature of the coiled-coil motifs provides a coupling/ cross-linking strategy that allows for higher-order protein cage assembly with precise control  $^{35,36}$ , nanoparticle assembly  $^{37}$ , cargo encapsulation  $^{38,39}$ , protein-polymer conjugation for polymer therapeutics  $^{40}$ , to name a few. They have found applications in targeted therapeutics, biosensors, affinity purification, nanostructures, and material designing  $^{34,41-43}$ 

P22-E3 and P22-K3 variants generated by fusing three repeats of E-coil (VAALEKE) or K-coil (VAALKEK) peptide sequences to the CP have resulted in the assembly of P22 particles into 3D structures where the particles are bridged by heterodimeric E- and K-coils on the two P22

variants.<sup>33</sup> Since heterodimeric coiled-coil motifs connect the VLP assembly through multivalent interparticle connections, the adjacency of the two variants is enforced in the 3D assembly by design. However, the dependence of the P22 particle assembly on the capsid morphology and the ionic strength of the medium (robustness), and the structural information of the higher-order assembly including the packing order of VLPs have not been explored. Here, we have examined the structural aspects of the coiled-coil mediated P22 PMF assembly – including the impact of particle morphology, resultant material robustness, assembly and packing of particles within the PMF lattice, and have utilized the knowledge gained from to build a functional PMF capable of single and multi-step catalysis.

### MATERIALS AND METHODS

DNA primers and oligonucleotides were ordered from Integrated DNA Technologies (Coralville, IA). *E. coli* BL21(DE3) electro and chemical competent cells were purchased from Lucigen (Madison, WI). DNase, RNase, lysozyme, AEBSF (4-(2-Aminoethyl)benzenesulfonyl fluoride hydrochloride) protease inhibitor solution, reduced nicotinamide adenine dinucleotide (NADH), NAD+, 2,2'-(ethylenedioxy)bis(ethylamine), ethylenediamine, EDC, and resazurin were purchased from Sigma Aldrich (St. Louis, MO). Polyamidoamine (PAMAM) dendrimers were purchased from Sigma Aldrich and Dendritech (Midland, MI). Phenazine methosulfate (PMS) was purchased from Chem-Impex International (Wood Dale, IL). Acetoin was purchased from Acros Organics (NJ). The chemical reagents for the buffer preparation, protease inhibitor tablets, and dialysis membranes were purchased from Fisher Scientific (Pittsburgh, PA). Alexa Fluor 488 C<sub>5</sub> maleimide, Texas Red C<sub>2</sub> maleimide, fluorescein-5-isothiocyanate (FITC), and EnzChek Phosphate Assay Kit were purchased from Invitrogen (Waltham, MA). Lucifer Yellow

Cadaverine was purchased from Biotium (Fremont, CA). Nanofiltration membranes were purchased from Sterlitech (Auburn, WA).

### **Expression of P22-E3 and P22-K3 (without enzymes)**

*E. coli* cells harboring the pRSFDuet-1 expression vector containing the truncated SP (residues 141-303, denoted as SP<sub>141</sub>) in MCS1, and P22 CP (either CP-E3 or CP-K3) in MCS2<sup>33</sup> were grown in 1 L of LB at 37 °C, while shaking at 200 rpm, in the presence of kanamycin (30  $\mu$ g/mL) to exert selection pressure. Protein expression was induced by addition of IPTG (0.5 mM, final) once the cells reached OD<sub>600</sub> = 0.6-0.8. The cultures were grown an additional 4 hrs after the induction with IPTG, and then, the cells were harvested by centrifugation at 4500 x g for 15 min at 4 °C. The harvested cell pellets were stored at -80 °C until subjected to purification of the proteins.

### Expression of PtDH@P22-E3 and AdhD@P22-K3

A combination of two vectors, pRSFDuet-1 (containing P22 CP-E3 or P22 CP-K3 in MCS2, but no SP<sub>141</sub> in MCS1), and pBAD containing the genes for PtDH-SP<sub>141</sub> or AdhD-SP<sub>141</sub> were cotransformed into *E. coli* BL21(DE3) cells, respectively. The transformed cells were grown on LB agar plates supplemented with kanamycin (30 μg/ mL) and ampicillin (100 μg/ mL) overnight at 37 °C to select cells transformed with both vectors. A single colony from each plate was picked and grown in 10 mL LB medium at 37 °C in the presence of kanamycin and ampicillin overnight. The overnight cultures were used to inoculate a 1 L LB medium supplemented with both antibiotics to exert selection pressure on both plasmids, and grown at 37 °C, while shaking at 200 rpm. Enzymatic cargo (PtDH-SP<sub>141</sub> or AdhD-SP<sub>141</sub>) expression was induced with L-arabinose (13.3 mM, final concentration) once the cells reached OD<sub>600</sub> = 0.6-0.8, and continued

incubation at 37 °C for 4 hrs. P22 CP (E3 or K3) expression was induced with IPTG (0.5 mM, final concentration) and continued growing at 30 °C overnight. The cells were harvested by centrifugation at 4500 x g for 15 min at 4 °C and the cell pellets were stored at -80 °C until subjected to purification of the proteins.

# **Purification of P22 VLP variants (with and without enzymes)**

The frozen cell pellets were thawed and resuspended in a buffer (50 mM sodium phosphate, 100 mM sodium chloride, pH 7.0), treated with DNase, RNase, lysozyme, AEBSF (0.2 mM, final concentration) and protease inhibitor tablets, and incubated at room temperature for 45 min, while rocking. The cell suspensions were lysed by sonication (2 min at 50% amplitude; Branson Digital Sonifier). The sonication process was repeated three times on ice and centrifuged at 12000 x g for 45 minutes at 4 °C. The supernatants were then loaded on to a 35% (w/v) sucrose cushion and ultracentrifuged at 45,000 rpm for 50 min at 4 °C, using a FiberLite F50L-8X39 rotor on a Sorvall WX Ultra 80 Series Centrifuge. The resulting protein pellet was resuspended in PBS (50 mM sodium phosphate, 100 mM sodium chloride, pH 7.0) and purified over an S-500 Sephadex (GE Healthcare Life Sciences) size exclusion column using a BioRad Biologic DuoFlow FPLC running at 1.0 mL/min. For the purification of P22-K3 VLPs, the samples were run through the size exclusion column using a high salt phosphate buffer (50 mM sodium phosphate, 500 mM sodium chloride, pH 7.0) at 1.0 mL/min. Eluted fractions containing P22 VLPs were pooled, concentrated by ultracentrifugation, and resuspended in approximately 3 mL of PBS. After resuspending P22-E3 and P22-K3 VLPs in PBS, the protein samples were supplemented with protease inhibitors and 1 mM EDTA to mitigate the cleavage of E- or K-coils attached to the CP.

# Assembly of P22-E3 and P22-K3 at various ionic strength conditions

P22-E3 and P22-K3 were buffer exchanged to the following buffers (Table 1) with varying ionic strengths (all buffers were at pH 7.0) and the concentration of each VLP variant was adjusted to 1 mg/ mL. A volume of 50 uL from each VLP variant was mixed with each other and incubated at room temperature for 1 hr. The  $OD_{600}$  (Agilent 8454 UV-vis spectrophotometer) of the samples were recorded. All the measurements were collected in triplicates.

Table 1. The compositions of different buffers used in the study with varying ionic strengths.

Ionic strength / mM	Sodium phosphate / mM	Sodium chloride / mM
4600	50	4494
4000	50	3894
3000	50	2894
2000	50	1894
1500	50	1394
1000	50	894
750	50	644
500	50	394
206	50	100
106	50	0
21	5.1	10.2

# **Small-Angle X-ray Scattering measurements**

The concentration of all the VLP samples were adjusted to 1 mg/ mL in the buffers described in table 1. The buffers used for background subtraction matched the respective buffer conditions of each sample. The measurements were taken at the Advanced photon source (APS) at the Argonne National Laboratories (12-ID-B beamline at 13.3 keV). A volume of 130 uL of each

sample was injected and continuously agitated by a syringe pump to minimize the radiation damage and prevent sedimentation. The Eiger 9M detector was used to collect 20 scattering patterns of each sample. One-dimensional scattering profiles were obtained by averaging two-dimensional scattering patterns. The data were presented as scattering intensity, I(q) versus the scattering vector, q, given by the following equation,

$$q = (4\pi \sin \theta)/\lambda$$

where  $\theta$  is half of the scattering angle  $2\theta$ , and  $\lambda$  is the wavelength used to acquire the measurements.

For the measurements involved heating, the samples were heated in a heat block at 60 °C for 30 mins and the measurements were taken. They were measured again after the samples were cooled back down to the room temperature.

### **Super-resolution 3D-Structured Illumination Microscopy (SR 3D-SIM)**

Fluorescent-labeled P22-E3 (with Alexa Flour 488) and P22-K3 (with Texas Red) prepared in PBS (I = 206 mM, pH 7.0) were mixed with each other after adjusting the concentration of each VLP to 1 mg/ mL. The sample was incubated at room temperature for 1 hr. The assembled sample was imaged using the DeltaVision OMX-SR 3D-SIM (Cytiva) equipped with a 1.42 NA Olympus 60X oil objective.

The assembled sample was diluted (8x) in the same buffer and 6.5 uL of the diluted sample was spotted on a no. 1.5 microcover glass (22 mm x 22 mm) just before imaging. A microscope slide (75 mm x 25 mm) was gently placed on the cover glass with the sample, avoiding air bubbles.

Immersion oil with a 1.516 reflective index was used when the sample cover glass was mounted

on the microscope. Laser lines of 488 nm with emission filters of 500–550 nm, and 561 nm with emission filters of 609–654 nm were used for collecting Alexa Fluor 488, and Texas Red signals, respectively. The z-axis section spacing was 0.125 μm. Fluorescent images of the VLP assemblies were acquired using DeltaVision-OMX image acquisition software, while the images were reconstructed using softWoRx image processing software. Collected fluorescent images were processed in terms of brightness and contrast using ImageJ software (version 2.1.0/1.53c).

### Monitoring the PtDH activity of PMF and P22-E3 particles

PtDH@P22-E3 (60 nM VLP) and P22-K3 (60 nM VLP) were mixed in PBS (I = 206 mM, pH 7.0) and incubated for 2 hrs to assemble the PMF. The encapsulated enzyme concentration was determined using A<sub>280</sub> under denatured conditions (in 6 M guanidine hydrochloride, using extinction coefficients, 33920 M<sup>-1</sup> cm<sup>-1</sup> for PtDH-SP<sub>141</sub>, and 44920 M<sup>-1</sup> cm<sup>-1</sup> and for P22 CP-E3). and number of PtDH enzymes per particle (105) calculated by the molecular weight values determined using SEC-MALS as previously described.<sup>25</sup> The PMF was centrifuged under gentle conditions (5000 x g, 3 mins), and the supernatant was recovered to determine the PtDH-SP<sub>141</sub> concentration in the supernatant (from unassembled PtDH@P22-E3) to measure that in the assembled material using an activity-based method. This was determined by comparing the rates of reactions between PtDH@P22-E3 (from the recovered supernatant vs. with a known concentration of enzyme, 2 uM) and 10 uM NAD<sup>+</sup>. The enzyme concentration was kept constant in the PMF and free particle reactions with the NAD(H)-dendrimer conjugates. The PtDH enzymatic reaction with NAD+ was monitored using a reporter reaction, resazurin, which involves a secondary catalyst, phenazine methosulfate (PMS), catalyzing NADH-dependent reduction of resazurin to fluorescent product resorufin, recycling NAD<sup>+</sup> for PtDH.<sup>44</sup>

The pelleted PMF was resuspended in I = 41 mM buffer (10 mM sodium phosphate, 20 mM sodium chloride, pH 7.0). The resuspended PMF in the kinetics reaction was adjusted to contain approximately 60 nM of P22 VLPs in a 100 uL volume. For the reactions containing PtDH@P22-E3 particles, P22 VLP concentration was adjusted in I = 41 mM buffer to contain the same PtDH enzyme concentration as in PMF reactions (3.1 uM, final). Both PMF and PtDH@P22-E3 particles were incubated with modified NAD(H) molecules overnight in the dark, with a total NAD concentration (calculated by considering both A<sub>265</sub> and A<sub>340</sub> measurements;  $\varepsilon_{265,NAD^{+}} = 18 \text{ mM}^{-1} \text{ cm}^{-1}$ ,  $\varepsilon_{265,NADH} = 14.4 \text{ mM}^{-1} \text{ cm}^{-1}$ , and  $\varepsilon_{340,NADH} = 6.22 \text{ mM}^{-1}$ cm<sup>-1</sup>) adjusted to 10.5 uM (final), which contributes to a ratio of 320 G2 dendrimers per VLP (and 150 G1.5 dendrimers per VLP) in PMF reactions. It is possible that the extinction coefficients of NAD(H) in the conjugates are different, and since we are mainly comparing the reactivities between free particles and PMF with each type of conjugate, this difference is neglected. To monitor the modified NAD<sup>+</sup> substrate reduction catalyzed by PtDH (in PMF or in P22-E3 free particle system), the reaction was initiated by mixing the modified NAD(H) substrate - enzyme mixture with a pre-mixed solution of 0.5 mM PMS, 2 mM sodium phosphite, and 0.5 mM resazurin. Fluorescence was monitored over a period of 1 hr using Cytation 5 multimode microplate reader (Ex: 544 nm, Em: 590 nm) operated using Gen5 software to analyze the reaction rates. The plate was shaken in-between measurements to avoid the sedimentation of the assemblies (for PMF reactions). The rate of a mock reaction, only containing modified NAD(H) substrates, PMS, sodium phosphite, and resazurin (no PtDH) in the same concentrations as in main PtDH enzymatic reactions was subtracted from that of the main enzymatic reactions to account for the non-enzymatic degradation of NADH. All reactions were performed in triplicates.

### Monitoring the PtDH-AdhD coupled enzyme activity of PMF

PtDH@P22-E3 (60 nM) and AdhD@P22-K3 (60 nM) were mixed in PBS (50 mM sodium phosphate, 100 mM sodium chloride, I = 206 mM, pH 7.0) and incubated for 2 hrs to assemble the PMF. The PMF was centrifuged under gentle conditions (5000 x g, 3 mins), and the supernatant was removed and replaced with 25 mM Tris buffer, pH 7.2 to resuspend the PMF. This step was repeated to remove any residual phosphate (from the PBS) remaining with the PMF and the final assembly was resuspended in 25 mM Tris buffer, pH 7.2.

To monitor the coupled enzyme activity, phosphate production was monitored using EnzChek Phosphate Assay Kit in Tris buffer (25 mM Tris, 38 mM NaCl, pH 7.2) to adjust the final ionic strength to 41 mM. The reaction contains (in a 100 uL total volume) 3.4 nM P22 VLPs (from PMF, resuspended in 25 mM Tris buffer, pH 7.2), 100 uM unmodified (free) NADH, 20 mM acetoin, 1 mM sodium phosphite, 200 µM 2-amino-6-mercapto-7-methylpurine riboside (MESG, assay substrate), and 1 U/mL purine nucleoside phosphorylase (PNP), where the concentrations of MESG and PNP were adjusted according to the manufacturer's recommendation. The kinetics of the reaction was monitored by A<sub>360</sub> in a Cytation 5 multi-mode microplate reader. The plate was shaken in-between measurements to avoid the sedimentation of the assemblies. A single enzyme free particle control reaction was carried out with PtDH@P22-E3 particles containing approximately the same PtDH enzyme concentration as in the PMF reaction. To remove the background rate, a mock reaction was performed without PMF or PtDH@P22-E3 free particles. The data were normalized by correction from A<sub>360</sub> at time zero and the rate of the mock reaction according to the following equation. All reactions were performed in triplicates.

Corrected 
$$\Delta A_{360} = (A_{360,t} - A_{360,t=0}) - (A_{360,mock,t} - A_{360,mock,t=0})$$

#### RESULTS AND DISCUSSION

### Coiled-coil mediated PMF assembly

To create a P22-based PMF utilizing coiled-coil peptide motifs as interparticle bridging linkers (Figure 1a), we used surface-modified P22 variants, P22-E3 and P22-K3. The P22-E3 and P22-K3 variants were created by fusing the C-terminus of P22 CP with three repeats of E-coil and Kcoil sequences, respectively, and incorporating the modified CP genetic constructs into a pRSFDuet-1 vector containing the gene for the truncated SP (residues 141-303, hereafter referred to as SP<sub>141</sub>).<sup>33</sup> The co-expression of the modified P22 CP (CP-E3 or CP-K3) and SP<sub>141</sub> in E. coli resulted in the in vivo self-assembly of P22 variants (P22-E3 or P22-K3 particles), which were subsequently purified. The presence of the P22 CP (49.16 kD for CP-E3 and 49.23 kD for CP-K3) and SP<sub>141</sub> (20.3 kD) in the assembled particle sample was verified using sodium dodecyl sulfate-polyacrylamide gel electrophoresis (SDS-PAGE) analysis, which showed clear bands with the expected molecular weights (Figure S1a). When the negatively stained particles were visualized by transmission electron microscopy (TEM), the micrographs revealed a monodispersed population of capsids having a similar diameter ( $56.87 \pm 3.31$  nm for P22-E3 and  $58.47 \pm 2.59$  nm for P22-K3) and morphology to the 58 nm wild-type P22 procapsids (Figure 1b). Further analysis of the CP of the purified P22 variants by liquid chromatography-mass spectrometry (LC-MS) verified the P22-CP and the measured and deconvoluted masses matched well with the expected molecular weights of the different CP variants with the E3 or K3 peptide extensions (Figure S2a).

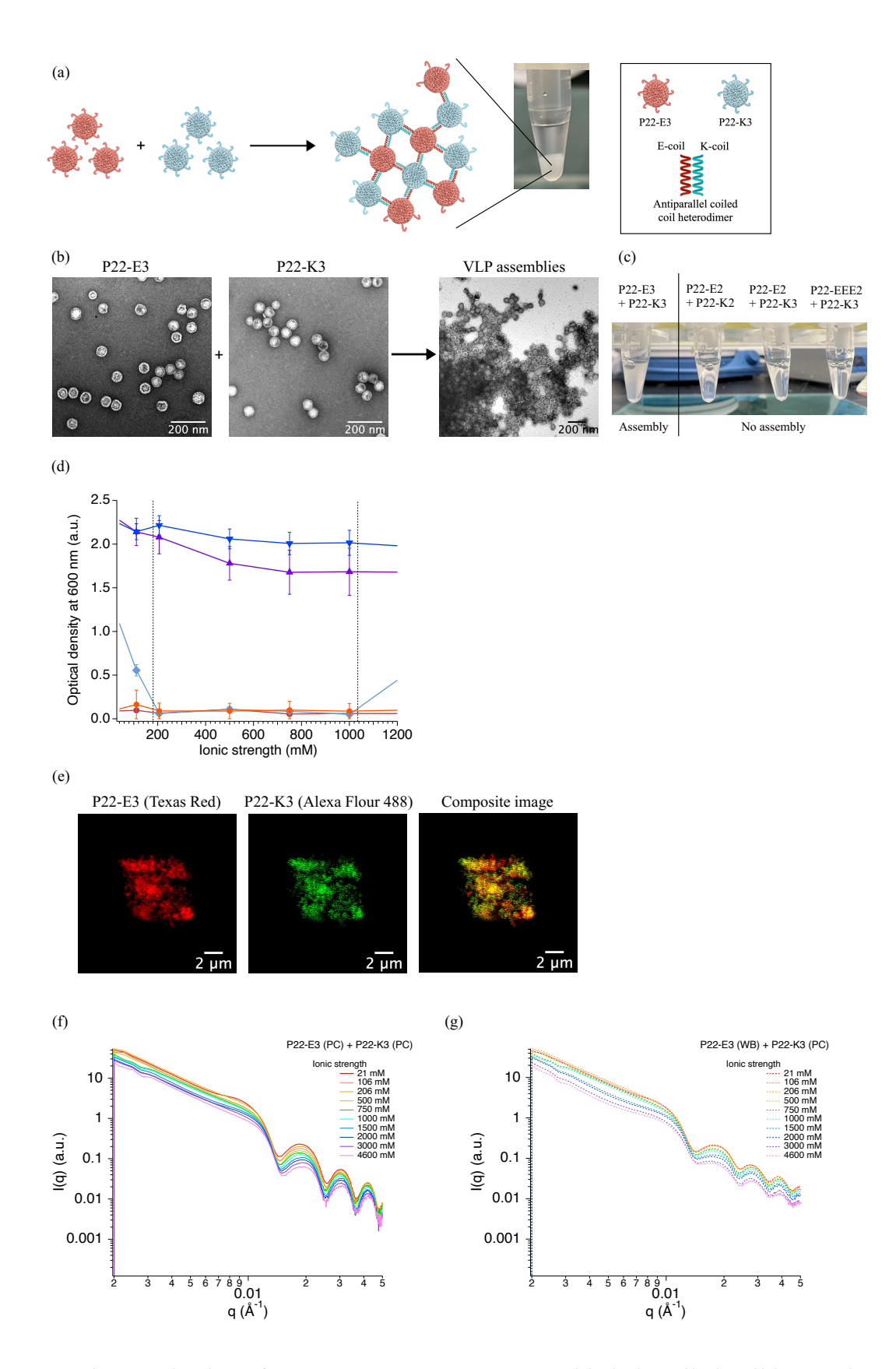


**Figure 1.** Characterization of P22-E3 + P22-K3 PMF assembled via coiled-coil interactions.

(a) Schematic showing the assembly between P22-E3 and P22-K3 particles into a PMF. (b) Negative stained transmission electron micrographs of P22-E3 (PC), P22-K3 (PC), and the assembled material. (c) Assembly behavior of different combinations of P22 variants, each containing a different number and/or sequence of coiled-coil motifs observed by the turbidity in the solution. Mixing of P22-E3 (PC) and P22-K3 (PC) resulted in instant turbidity, while P22-E2 and P22-K2, P22-E2 and P22-K3, and P22-EEE2 and P22-K3 combinations did not exhibit any turbidity upon mixing. (d) Assembly of P22-E3 (PC or WB) with P22-K3 (PC) under different ionic strength conditions examined by the optical density at 600 nm ( $OD_{600}$ ). Higher  $OD_{600}$ values indicate light scattering due to the formation of aggregates. All data points are expressed as mean  $\pm$  1 SD (n=3). This region represents the window of ionic strengths where individual particle controls do not self-aggregate, suggesting that the scattering observed for the mixtures is due to coiled-coil interactions guiding the two variants to assemble. (e) Super-resolution fluorescence microscope images of the PMF where the P22-E3 (PC), and P22-K3 (PC) are labeled with Texas Red, and Alexa fluor-488 fluorescent dyes, respectively, revealing that two variants are evenly distributed in the assembled material. Small-angle X-ray scattering (SAXS) analysis of the PMFs, (f) P22-E3 (PC) + P22-K3 (PC) and (g) P22-E3 (WB) + P22-K3 (PC) assembled at different ionic conditions.

When the P22-E3 and P22-K3 were combined at room temperature (in 50 mM sodium phosphate, 100 mM NaCl, at pH 7; equivalent to I = 206 mM) an instant turbidity was observed upon mixing indicating a rapid assembly of VLPs, consistent with previously reported behavior of these variants (Figures S3 and 1c). All the assemblies tested in this study were prepared by combining equimolar populations of different P22 variants. To explore the assembly behavior of P22-E3 and P22-K3 procapsids at a range of ionic strength conditions, both types of P22 VLPs

were mixed in buffers with various ionic strengths, ranging from I = 21 mM to I = 4600 mM at room temperature and the optical density measured at 600 nm (OD<sub>600</sub>) to monitor the assembly (Figures 1d, and S4). Control experiments containing only the P22-K3 showed turbidity at I < 206 mM and I > 1 M, while the P22-E3 particle control was turbid only at I > 2 M. This behavior of the individual particles is likely due to the salting in and out of the proteins at low and high ionic strengths, respectively. At every ionic strength tested the mixture of P22-E3 and P22-K3 became instantly turbid (Figures 1d, and S4), suggesting that the coiled-coil assembly between particles is stable over the range of ionic strengths we examined. Importantly, within the window of I = 206 mM to I = 1 M ionic conditions, where all subsequent PMF assemblies were conducted (Figure 1d) (to actively avoid the unwanted self-aggregated assemblies in addition to the coiled-coil binary assemblies), the absence of turbidity in the individual particle controls suggests that the scattering observed for the mixture is due to the interparticle assembly between E3- and K3-coils resulting in a P22-based PMF.

The available structural data on P22 CP does not include the location of C-terminus of CP, however, experimental data suggests that the C-terminus is exposed to the exterior of the procapsid. Because the PC particles undergo a dramatic morphology transition, upon expansion, the location of the C-terminus of CP might be different from that of PC. Therefore, to explore how would the morphology transition would impact the orientation of coiled-coil peptide motifs, thus their dimerization, we prepared the WB morphology of P22-E3 particles by heating the P22-E3 PCs at 75 °C. The complete expansion of PC into WB morphology was confirmed using native agarose gel electrophoresis (Figure S5). When the WB of P22-E3 and PC of P22-K3 were mixed at the same range of ionic strengths (I = 21 mM to I = 4600 mM) at room temperature to measure the OD<sub>600</sub>, the observed scattering values exhibited a similar trend as when both types of

particles were in the PC morphology (Figures 1d, S3 and S4). This overall observation suggests that the interparticle assembly due to coil-coil peptide interactions on the exterior of the capsid, does not depend on the particle morphology, and can potentially be used to form assembled materials using all three P22 morphologies (PC, EX, WB). This is an added advantage of the coiled-coil PMF system compared to other P22-based PMFs created with the ditopic Dec-Dec linkers as the latter requires the expansion of P22 procapsids into EX or WB morphologies because Dec-Dec linker only binds to these mature P22 morphologies. The requirement of the EX or WB morphologies in creating Dec-Dec based PMFs might not always be pragmatic, as these morphology transitions require heat or SDS, conditions where encapsulated enzymes might be less stable with loss of catalytic activity. However, the P22 PMFs generated via coiled-coil motifs do not have this limitation as both morphologies can be used to construct coiled-coil based P22 PMFs even with more delicate enzymes.

To test if the multivalency of the coiled-coil interactions on the capsid exterior might aid in the 3D structural assembly of P22 particles, two other variants of P22, made by the fusion of only two repeats of E- and K- coils to the CP (P22-E2 and P22-K2)<sup>31</sup> (characterization data are shown in Figures S1a, S2) were mixed under similar ionic strength conditions, I = 206 mM. No interparticle assembly was observed for the P22-E2 and P22-K2 mixture (Figures 1c and S3). Higher-order assembly between P22-E2 and P22-K2 has been reported previously but only with the addition of linker molecules such as positively charged PAMAM dendrimers. Our observation suggests that P22-E2 and P22-K2 do not assemble via a coiled-coil interaction. Also, when we tested the assembly between P22-E2 and P22-K3 no scattering at 600 nm was observed, suggesting 2 and 3 repeats of E- and K- coil sequences, respectively, are not sufficient to form coiled-coil heterodimers bridging the two types of VLPs. In a separate experiment, we

tested the assembly between P22-K3 and another construct, P22-EEE2. Unlike P22-E3, the CP of P22-EEE2 is only fused with two repeats of rather more negatively charged heptapeptide (VAALEEE) (characterization data are shown in Figures S1a, S2). When P22-EEE2 and P22-K3 were mixed at the same salt conditions, I = 206 mM, the mixture did not show any scattering at 600 nm, suggesting no assembly between particles (Figures 1c and S3). Altogether, the lack of assembly between any particles bearing a two heptapeptide repeat, P22-E2 and P22-K2, P22-E2 and P22-K3, and P22-EEE2 and P22-K3, suggests that at least three repeats of the heptapeptide in the coiled-coil motif, with hydrophobic and hydrophilic amino acids in the corresponding positions, are required to initiate the formation of coiled-coil heterodimers to generate higher-order P22 VLP assemblies. Previous studies<sup>45, 46</sup> reporting the minimum chain length, or the number of residues required for the formation of a stable coiled-coil precede our observation.

To explore the P22-E3 and P22-K3 particle locations in the 3D PMF structure, we labeled P22-E3 and P22-K3 procapsids with red (Texas Red) and green (Alexa Flour 488) fluorescent molecules, respectively. The labeled particles were mixed with each other at I = 206 mM, and the resultant assembled material was viewed under a super-resolution fluorescent microscope. The fluorescence micrographs revealed the formation of assemblies (approximately 2-6 um in size) with red and green colors randomly positioned within the assemblies. This suggests that the two types of P22 particles are evenly distributed in the PMF (Figure 1e). Since the particles are bridged by the E3- and K3- heterodimeric coiled-coils there is an enforced adjacency of the two types of P22 VLPs in the PMF.

### SAXS analysis of the coiled-coil based PMF

The structure of the P22-E3 + P22-K3 assembled material was analyzed further using small angle X-ray scattering (SAXS). P22-E3 (PC or WB) and P22-K3 (PC) samples mixed at each ionic condition were analyzed by SAXS. They exhibited broad peaks regardless of the ionic strength or VLP morphology, indicating that the arrangement of the VLPs in the PMF has no long-range order at every condition tested (Figures 1f, g). SAXS profiles obtained for the mixtures exhibited a shift of the first minima (at  $q \approx 0.015 \text{ Å}^{-1}$ ) to higher q region with increased ionic strengths (Figures 1f, 1g, and S6a). The fact that the individual particle controls also showed this general trend of minima shift to higher q (Figures S6a-d) suggests that it is not likely due to a PMF structural change observed with the increased ionic strength, but rather due to a change in the form factors of individual VLPs with the increased solvent ion density. This could be a result of counter ions and ion layers localized at the highly charged exterior surfaces of the particles. The observed form factors for P22-E3 (PC) and P22-K3 (PC) particles, within their non self-aggregating ionic strength window (I = 206 to I = 1000 mM), were different, suggesting that they have different electron densities around their shells. The difference observed for P22-E3 (PC) and P22-K3 (PC) particles are explained in the supplementary material (Supplementary discussion-Section 1a).

The linear intensity profile at low q region can be used to assess the particle packing nature of the aggregates (Figures 1f-g) in double-logarithmic plots and is explained in the supplementary material (Supplementary discussion-Section 1b). Incline data suggest that P22-K3 self-aggregates are relatively more densely packed than P22-E3 self-aggregates or the PMF which are fractal/ porous in nature. There are six positively charged residues per K3 coil (and 420 K3 coils per particle) on a highly negatively charged VLP surface, which could result in strong electrostatic interparticle self-interactions, thus dense aggregation of P22-K3.

To investigate the impact of temperature on the PMF structure, we heated the PMFs assembled at I = 206 mM and I = 1 M to 60 °C for 30 mins and took SAXS measurements at 60 °C, and after they were cooled back down to room temperature (Figure S9). At 60 °C, the structure of the PMF was retained, highlighting the robustness of the PMF. However, the individual particles undergo an irreversible morphology transition from PC to an expanded morphology at 60 °C (Figure S10 and Supplementary discussion-Section 1c).

To explore the impact of the ionic strength modulations on the structure of the PMF, we analyzed the P22-E3 (PC) + P22-K3 (PC) mixtures assembled at I = 206 mM and I = 1 M in terms of their responses to the changes in ionic strengths (Figure S11). The PMF assembled at I = 206 mM was diluted with water to lower the ionic strength to I = 41 mM, and SAXS profiles before and after dilution were compared. The intensity profiles obtained after diluting to I = 41 mM were similar to that before dilution at I = 206 mM for both the mixture and P22-E3 particle control (Figure S11a). This suggests that once the two P22 variants are assembled into the PMF at I = 206 mM, the structure of the PMF is retained at I = 41 mM. In contrast, the intensity profile of P22-K3 was linear at the low q region upon dilution, suggesting their homogenous self-aggregation at I < 206 mM, which is consistent with the previous observations (Figures S4 and S6d). This is important as we conducted the subsequent partitioning and kinetic experiments at I = 41 mM, with the PMF assembled at I = 206 mM, rather than mixing the two P22 variants directly at I = 41 mM, to avoid the presence of any independently self-associated P22-K3 particles in the final assembled material.

The PMF assembled at I = 1 M was subjected to a series of ionic strength modulations including increasing the ionic strength to I = 2 M, followed by dilution with water to lower the ionic

strength back to I = 1 M. The measured intensity profiles and the first peak minima at all these ionic strength conditions remained the same. Conversely, the first peak minimum of PMF directly assembled at I = 2 M was slightly different from that of the PMF of which the ionic strength was increased to I = 2 M from I = 1 M (Figure S11b). This observation further confirms that the structure of PMF, once assembled, is highly stable and resistant to changes in ionic strength. P22-E3 individual particle control did not exhibit any difference in the SAXS profiles in response to the same series of ionic strength modulations (Figure S11c), as P22-E3 does not self-aggregate at I < 2 M. In contrast, when individual P22-K3 particle control was subjected to the same sequence of ionic strength modulations, the intensity profiles at low q region switched between non-linear and linear trends at I = 1 M and I = 2 M, respectively (Figure S11d). This indicates the reversible self-aggregation and de-aggregation of P22-K3 at I = 2 M and I = 1 M, respectively, which is consistent with the previous data (Figures S4 and S6d). This observation suggests that individual particles are sensitive to the ionic strength modulations in contrast to the assembled PMF material which exhibits structural integrity across a wide range of conditions and is an example of a property of the higher-order material beyond that of the individual building blocks.

# Partitioning of fluorescent-labeled dendrimers into P22-E3 + P22-K3 PMF

The assemblies constructed from P22-E3 and P22-K3 procapsids, as well as P22-E3 WB and P22-K3 PC, carry a high net negative surface charge with measured zeta potentials of -19.9 mV and -17.8 mV, respectively (Table 2). The individual particles (building block units) carry net negative surface charges, but different in magnitudes as previously reported (Table S2).<sup>20</sup> We hypothesized that the net negative surface charge of the PMF would facilitate the localization of positively charged molecules within the PMF, while the negatively charged molecules would be

excluded. We measured the partitioning of fluorescent-labeled PAMAM dendrimers with different charges (negatively charged generation (G)1.5 and positively charged G2) into the charged PMF at low ionic strength (I = 41 mM), with varying input dendrimer concentrations to obtain a saturation binding curve. After preparing the PMF at I = 206 mM, they were isolated and incubated with the fluorescent-labeled dendrimers at I = 41 mM. After incubation with the dendrimer solutions, the PMF and the solution phases were separated by gentle centrifugation, and the fluorescence in the recovered supernatants was measured and compared to the input fluorescence before incubation with PMF, to calculate the fluorescence partitioned into the PMF phase. We analyzed their partitioning (binding) into the PMF in terms of accumulated dendrimers:P22 as a function of varying input dendrimer:P22 ratios (Figure S12). Positively charged G2 dendrimer exhibited higher levels of partitioning into the PMF at every input dendrimer concentration than the negatively charged G1.5 dendrimer, and the level of partitioning increased with the input dendrimer concentrations.

Assembly	Zeta potential (mV)
P22-E3 (PC) + P22-K3 (PC)	$-19.9 \pm 3.1$
P22-E3 (WB) + P22-K3 (PC)	$-17.8 \pm 3.7$

**Table 2.** Zeta potential values of the assemblies made of P22-E3 (PC or WB) + P22-K3 (PC). Both types of assemblies exhibit a net negative charge.

We tested the partitioning of fluorescent-labeled dendrimers with different charges and sizes into the PMF at I = 41 mM. The amount of different dendrimers, and thereby the number of dendrimer charge groups introduced in each partitioning reaction were based on the ratio of 320 G2 dendrimers per particle (5120 dendrimer surface charge groups per P22) as higher amounts of G2 dendrimers cause aggregation of the negatively charged VLPs. To evaluate the distribution of

dendrimers between the supernatant and PMF, the fluorescence intensity in the two phases after incubation were used to obtain a partitioning coefficient (*P*) to quantify the concentration of charged dendrimer partitioned from bulk solution into the highly charged PMF phase. Since PMF is an amorphous and a fractal aggregate, a precise volume for the PMF phase cannot be expressed. The physical volume of the PMF was estimated to be 2 uL after pelleting down and isolating the PMF (Figure S13). The volume of the supernatant phase was 1 mL, and the volumes of the PMF and the supernatant phases were considered when expressing the *Log P* for each dendrimer according to the following equation.

$$Log P = Log_{10} \left( \frac{[Dendrimer] in PMF}{[Dendrimer] in Supernatant} \right)$$

Higher  $Log\ P$  values were obtained for the positively charged dendrimers (G2, G4, and G6), indicating that positively charged dendrimers preferentially distributed into the negatively charged PMF phase over the supernatant, as expected (Figures 2a and S14a, c). For the G2 dendrimer, we saw approximately an equal distribution of G2 molecules between the two phases (approximately 50% of the input dendrimers partitioned into the PMF phase). The partitioning of the G4 and G6 dendrimers into the PMF was similar but significantly higher than that of G2. This is likely due to the higher number of positive charge groups in G4 (64) and G6 (256), as opposed to 16 charge groups in G2, causing the former to experience stronger attractive forces to the negatively charged VLP assembly. In contrast, the negatively charged dendrimers (G1.5, G3.5, and G5.5) exhibited lower  $Log\ P$  values (Figures 2a and S14b, c). Note that  $Log\ P > 0$  suggests a higher dendrimer concentration in the PMF than in the supernatant, not a higher amount. Even a partitioning of 10% of the input dendrimers into PMF (with 2 uL of volume) from bulk (leaving 90% of the dendrimers in the supernatant with a volume of 1 mL) would

generate a Log P value of ~1.8, which was observed for every negatively charged G1.5, G3.5, and G5.5 dendrimers. Taken together, these data suggest that electrostatic interactions can be used to control the partitioning and exclusion of charged macromolecules into or out of the charged 3D VLP assemblies, but with lower selectivity than previously reported PMF materials.<sup>12</sup>

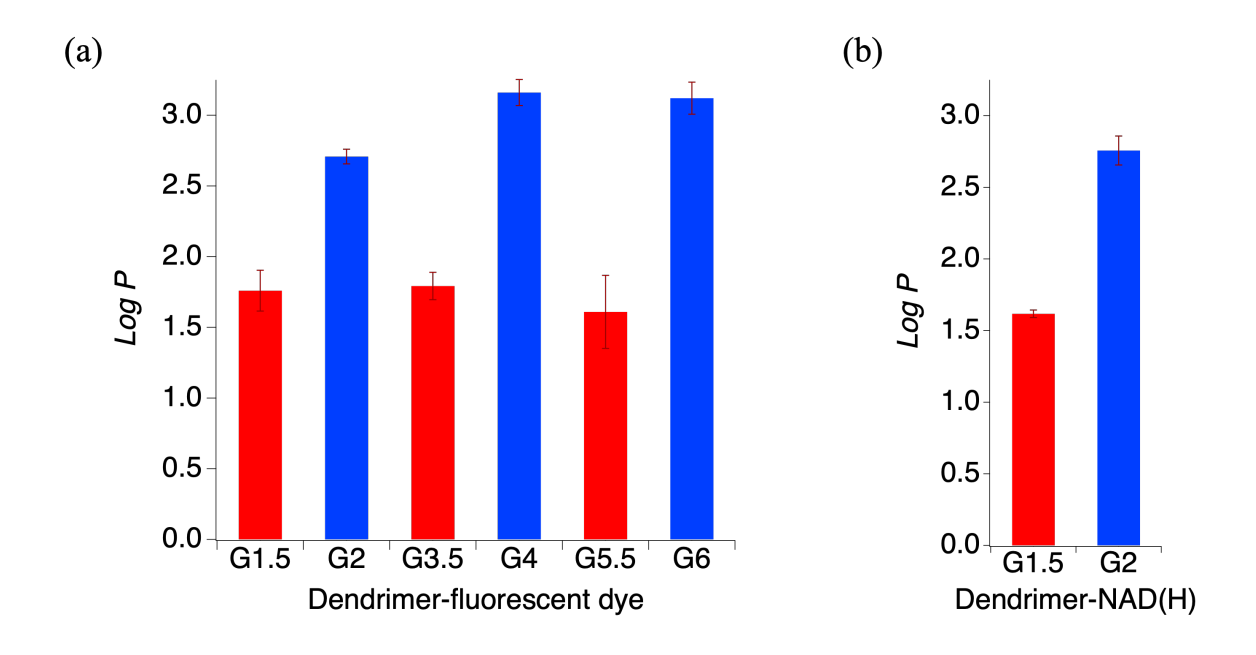


**Figure 2.** Analysis of charged macromolecules partitioning into the PMF. (a) Partitioning of fluorescent-labeled PAMAM dendrimers with different charges and sizes into the highly negatively charged PMF at low ionic strength (I = 41 mM), expressed as the log of the calculated partitioning coefficient (P). Positively and negatively charged dendrimers are labeled with fluorescein-5-isothiocyanate (FITC) and Lucifer Yellow Cadaverine fluorescent molecules, respectively. (b) Partitioning analysis of the dendrimer generations 1.5 (negative) and 2 (positive), labeled with NAD(H) into the PMF at I = 41 mM. All data points are expressed as  $mean \pm 1 \text{ SD } (n=3)$ .

### Partitioning of dendrimers labeled with NADH into P22-E3 + P22-K3 PMF

To evaluate the partitioning of a charged enzymatic substrate into the PMF we modified NAD(H), a cofactor for the enzyme, phosphite dehydrogenase (PtDH). We attached PAMAM dendrimers to the NADH using dendrimer G1.5 (negatively charged) and G2 (positively charged), as these are small enough to access the interstitial space in the PMF and also small enough to pass through the pores in the P22 PC accessing any encapsulated enzymes.<sup>47</sup> To analyze the partitioning of NADH modified with the charged dendrimers into the PMF, we used the characteristic absorbances of both the NAD<sup>+</sup> and NADH to calculate the total NAD amounts before and after incubating with the PMF, at low ionic strength (I = 41 mM). The input dendrimer concentrations in the partitioning reactions were adjusted based on 320 G2 dendrimers per particle and followed a similar analysis to obtain a partitioning coefficient as mentioned above for the fluorescent-labeled dendrimers (Figure 2b). A total NAD amount was considered as the labeled NADH could get re-oxidized over time. The Log P values obtained for NADH<sub>G2</sub><sup>(+)</sup> and NADH<sub>G1.5</sub><sup>(-)</sup> were similar to that of the fluorescent-labeled dendrimers used in the above partitioning experiment. NADH<sub>G2</sub><sup>(+)</sup>exhibited a higher *Log P* over NADH<sub>G1.5</sub><sup>(-)</sup> indicating the preferential partitioning of NADH<sub>G2</sub><sup>(+)</sup> over NADH<sub>G1.5</sub><sup>(-)</sup>.

Both partitioning experiments involving fluorescent- or NADH-labeled dendrimers were carried out with the same input dendrimer charge groups per VLP ratios (320 G2 molecules or 5120 dendrimer surface groups per particle). However, for the kinetic study, for the comparison between NADH<sub>G2</sub><sup>(+)</sup> and NADH<sub>G1.5</sub><sup>(-)</sup>, we kept the NAD substrate concentration constant between reactions. Since the NADH-dendrimer labeling efficiency was different between the two dendrimers, the input dendrimer:capsid ratio varied between them (320 and 150 for G2 and G1.5 dendrimers per P22, respectively). According to the dendrimer saturation curve we obtained

(Figure S12), the partitioning of G1.5 dendrimer into the PMF at 150 input dendrimers:P22 ratio was similar, but slightly lower than that of 320 input G1.5 dendrimers:P22 ratio, further separating the extent of G1.5 dendrimer partitioning into the PMF from that of G2 dendrimer in the kinetic study. The actual input ratios of the two types of dendrimers used in the kinetic experiments, and their corresponding partitioning levels (accumulated dendrimers:P22 ratios) are shown in arrows in the saturation binding curve (Figure S12), displaying the difference of oppositely charged dendrimers partitioning into the negatively charged PMF.

### Catalytic activity of PtDH in the disordered PMF and free particles

To explore the impact of the charge of the substrates and their partitioning, on the activity of a highly charged amorphous catalytic PMF, we incorporated PtDH enzymes<sup>48</sup> through their encapsulation inside P22-E3 particles (characterization data are shown in Figures S1b, S2, and S15). We encapsulated PtDH-SP<sub>141</sub> fusion inside P22-E3 capsids, resulting in individual coreshell particles (PtDH@P22-E3, using core@shell nomenclature where the core is the cargo enclosed by the capsid shell). PtDH catalyzes the nearly irreversible oxidation of phosphite to phosphate using NAD<sup>+</sup> as an oxidizing agent.<sup>49</sup> We used a reporter reaction<sup>44</sup> with a secondary catalyst, phenazine methosulfate (PMS), which catalyzes NADH-dependent reduction of resazurin to the fluorescent product resorufin, thus recycling NAD<sup>+</sup>, to monitor the reduction of NAD<sup>+</sup> by PtDH (Figure 3a). However, PtDH is a delicate enzyme that loses its stability and optimum catalytic activity at high temperatures and after treatment with certain chemicals, such as SDS (Figure S16). Therefore, the catalytic activity of PtDH encapsulated in a P22-based PMF cannot be achieved as construction of Dec-Dec linker-mediated P22 PMF<sup>11, 12, 16</sup> requires heat (65-75°C) or SDS<sup>30</sup> to obtain VLPs in EX or WB morphology. Thus, the current PMF constructed via coiled-coil interactions between the capsids offers a unique and versatile

platform to investigate the catalytic behaviors of many enzymes which could lose optimum activity and stability under harsh conditions.

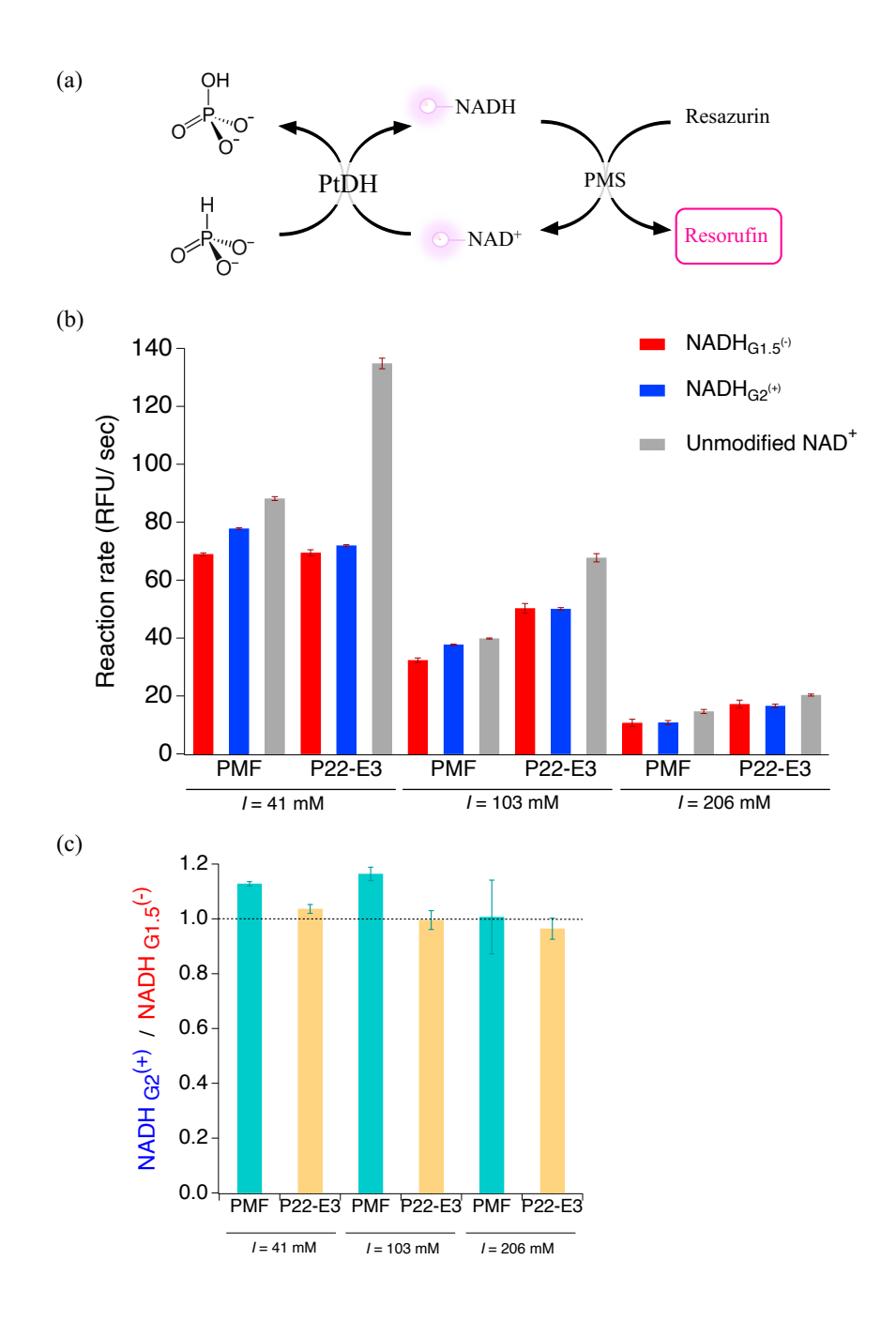


**Figure 3.** Catalytic activity of PtDH enzyme in PMF and P22-E3 free particles with modified NADH substrates. (a) Catalytic scheme of PtDH catalyzing the phosphite oxidation to phosphate using NAD<sup>+</sup> as an oxidant. The secondary catalyst, phenazine methosulfate (PMS), catalyzes the

oxidation of NADH, recycling NAD<sup>+</sup>, reducing resazurin to fluorescent product resorufin, which was used to monitor the PtDH enzyme activity in PMF and free particles (P22-E3). (b) The PtDH reaction rates expressed as relative fluorescent units (RFU)/ sec in PMF and P22-E3 free particles against NADH<sub>G1.5</sub><sup>(-)</sup> (red bars), NADH<sub>G2</sub><sup>(+)</sup> (blue bars), and unmodified (free) NAD<sup>+</sup> (grey bars) substrates at I = 41 mM, 103 mM, and 206 mM conditions. (c) The selectivity of PtDH enzyme (in PMF and P22-E3 free particles) towards reacting with oppositely charged NADH<sub>G2</sub><sup>(+)</sup> and NADH<sub>G1.5</sub><sup>(-)</sup> substrates at different ionic conditions, expressed as a ratio of reaction rates. A ratio above 1 (shown in a dotted line) indicates a preferential reactivity towards the positively charged NADH<sub>G2</sub> substrate. All data points are expressed as mean  $\pm$  1 SD (n=3).

We analyzed the reactivity of PtDH in free P22-E3 particles (unassembled) with the NADH<sub>G2</sub><sup>(+)</sup>, NADH<sub>G1.5</sub><sup>(-)</sup>, and unmodified (free) NAD<sup>+</sup> substrates. We did not conduct control experiments involving PtDH@P22-K3 particles as they self-aggregate at the low ionic condition (I = 41 mM, pH 7) (Figures 1d, S4, and S6d, S11a) where the main kinetic study was performed. We observed similar turnover rates for PtDH in free P22-E3 particles with NADH<sub>G2</sub><sup>(+)</sup> (72.0 ± 0.3 RFU/sec; RFU=relative fluorescence units) and NADH<sub>G1.5</sub><sup>(-)</sup> (69.4 ± 1.0 RFU/sec) without a clear differentiation between the two modified substrates (Figures 3b and S17). However, the turnover rates observed for unmodified NAD<sup>+</sup> substrates were faster (134.8 ± 1.8 RFU/sec) over the modified substrates likely due to the differences in overall cofactor size, cofactor mobility, thus their accessibility to the enzyme active site (Supplementary discussion-Section 2).

We used PtDH@P22-E3 particles, together with P22-K3 particles, to assemble an amorphous PMF via coiled-coil peptide interactions on the particle exterior surfaces. Since the P22 PMFs assembled from these coiled-coil interactions are highly negatively charged (Table 2), we hypothesized that preferential partitioning of positively charged substrates would result in an

increased local concentration of these substrates within the PMF, and possibly increase the reaction rates compared to negatively charged substrates. We kept the total PtDH concentration the same between individual P22-E3 particle reactions and PMF reactions (Figure S18). We saw differences in PtDH activity in the PMF when using dendrimer-modified and unmodified NAD substrates, likely due to the differences in accessing the enzymes (Figures 3b, S17, and Supplementary discussion-Section 2). Unmodified NAD+ exhibited faster rates (88.2  $\pm$  0.7 RFU/sec), as it has the potential to access the PtDH active site more readily than the NAD(H) substrates modified with bulky dendrimer groups. Thus, the comparison between modified and unmodified substrates depends on a number of factors including the overall cofactor size and PMF (and/or individual P22) porosity. Since the goal of this work was to explore the effects of differential partitioning of substrates modified with differently charged dendrimers on kinetics of a catalytic PMF, we compared the reaction rates of PtDH<sub>PMF</sub> materials in the presence of NADH<sub>G2</sub>(+) and NADH<sub>G1.5</sub>(-) at low ionic strength conditions (I = 41 mM, pH 7).

The reaction rates observed for PtDH<sub>PMF</sub> were  $77.8 \pm 0.3$  RFU/sec with the positively modified NADH (NADH<sub>G2</sub><sup>(+)</sup>) and  $68.9 \pm 0.5$  RFU/sec with the negatively modified NADH<sub>G1.5</sub><sup>(-)</sup> (Figure 3b). The observed 1.13 fold difference between the two NADH substrates suggested that, even though the positively charged G2 dendrimers exhibit a favorable partitioning into the PMF from the bulk, the negative G1.5 dendrimers also partition into the assembled phase to some extent at I = 41 mM, under the same input dendrimer concentrations (Figure 2). Therefore, the observation that the PtDH<sub>PMF</sub> reaction rate with NADH<sub>G2</sub><sup>(+)</sup> was only slightly higher than that of NADH<sub>G1.5</sub><sup>(-)</sup>, reflects the increased local concentrations of both substrates within the PMF, which could contribute to the similar reactivities, and only slight selectivity for NADH<sub>G2</sub><sup>(+)</sup>, and mirrors the trends observed in partitioning experiments (Figure 2).

The kinetic behavior of positively and negatively charged dendrimers with the unassembled PtDH@P22-E3 was very similar (Figure 3b and S19), and the PMF showed only slight selectivity towards the positively charged substrate (Figure 3b and c). The positively charged NADH<sub>G2</sub><sup>(+)</sup> substrates were found to interact with the negatively charged individual P22-E3 particles (Figure S20), thus complicating the comparison between positively and negatively charged substrates between free P22-E3 particles and PMF reactions (Supplementary discussion-Section 3).

Another factor, beyond partitioning of the substrate, that might play a role in the overall catalytic activity of the PMF is the relative mobility of the substrate within the PMF. The observation that in both individual P22 particles and in PMF the unmodified NAD<sup>+</sup> showed faster turnover than either of the bulk modified NAD(H) cofactors suggests that access and mobility might play a role; the porosity of the PMF and the migration of the substrate need to be considered. Low ionic strength favors increased partitioning of the charged substrate but simulations have revealed the possibility a less dynamic binding interaction (tight binding through fast on rate and slow off rate).<sup>31</sup> Since the PMF assembled through coiled-coils is a fractal aggregate, the interparticle distances can only be estimated from the structure of very similar E3- and K3- heterodimeric coiled-coils (measured at 3.7 nm)<sup>50</sup>, which suggests this as the closest VLP-VLP distance. Therefore, the space between VLPs is only slightly larger than the size of the G2 dendrimer (~2.9 nm in diameter) which might play a role in its migration within the PMF. Also, the charged substrates partitioned into the PMF might have low mobility due to strong electrostatic interactions. Therefore, we repeated the kinetic assays at higher salt concentrations (at I = 103mM and I = 206 mM), to increase mobility of the substrates inside the PMFs, due to charge screening, to probe the discrimination in kinetics between the charged substrates. With increased

ionic strengths, we also expected a lower partitioning of the substrates into the PMF. At I = 103mM, the PMF exhibited a selectivity towards partitioning, thus reactivity with the positively charged substrates over negatively charged substrates (Figures 3b and 3c), similar to the reactions conducted at I = 41 mM, but the selectivity was lost when ionic strength was raised to I= 206 mM (Figures 3b and 3c). The lack of catalytic substrate differentiation between PMF and unassembled particles, at any of the higher salt concentrations (Figures 3b, S17, and S19), is possibly due to steric hindrance faced by the modified substrates in the interstitial space restricting their mobility, even though the electrostatic interactions between substrate and capsid surfaces were screened. Free particle controls did not show any preference towards one charged substrate uptake over the other at these higher ionic strength conditions. The measured reaction rates decreased with the increased ionic strengths, which could be attributed to the lower partitioning coefficients obtained for the charged substrates (Figure S21), and the PtDH enzyme activity affected by the high salt concentrations. Therefore, increasing the ionic strength of the medium to obtain a better differentiation between the charged substrate partitioning and their mobility inside the highly charged PMF, compared to the free particle controls did not result in increased substrate selectivity in the PMF, suggesting that charge-based mobility of the substrate within the PMF was likely not a significant factor.

# PtDH-AdhD coupled catalytic activity in the disordered PMF

The interaction between the E3 and K3 modified P22 VLPs resulting in the coiled-coil heterodimer bridging imposes a potentially useful adjacency between the 2 different capsids within the 3D assembly. To take advantage of this, we modified the existing design to encapsulate a second enzyme, alcohol dehydrogenase D (AdhD)<sup>51</sup>, within the P22-K3 capsid and co-assemble the AdhD@P22-K3 (characterization data are shown in Figures S1b and S2) with

PtDH@P22-E3 to form a multi-enzyme catalytic material. This material could drive an enzymatic cascade reaction (Figure 4a) and demonstrate the utility of the coiled-coil based assembly for construction of VLP-based material capable of complex multi-step catalysis. Here, the NADH consumed by AdhD can be regenerated by PtDH (Figure 4a). We monitored the production of phosphate catalyzed by PtDH at I = 41 mM over time with unmodified (free) NADH, using a phosphate detection reaction monitored at 360 nm (Figure 4b) to evaluate the coupled catalysis process. The reaction of the PMF functionalized with PtDH and AdhD exhibited a faster increase in A<sub>360</sub> overtime, suggesting that the NADH is recycled back to NAD<sup>+</sup> by the second enzyme, AdhD, for the PtDH catalyzed phosphite oxidation. In contrast, the single enzyme free particle control (PtDH@P22-E3) exhibited a very slow increase of A<sub>360</sub> over time (Figure 4b), likely due to trace amounts of NAD<sup>+</sup> present in the NADH substrate solution, and the auto-oxidation of NADH to NAD<sup>+</sup> over time, slowly turning over PtDH enzyme catalyzing the phosphate production. We did not conduct a single enzyme free particle control reaction with AdhD@P22-K3, as it self-aggregates at the ionic condition where we performed the main kinetic study. The observation of the active two-step catalytic pathway driven inside the PMF highlights the potential of this robust coiled-coil based PMF as a versatile platform for the construction of functional biocatalytic higher-order materials driving multi-step reactions.

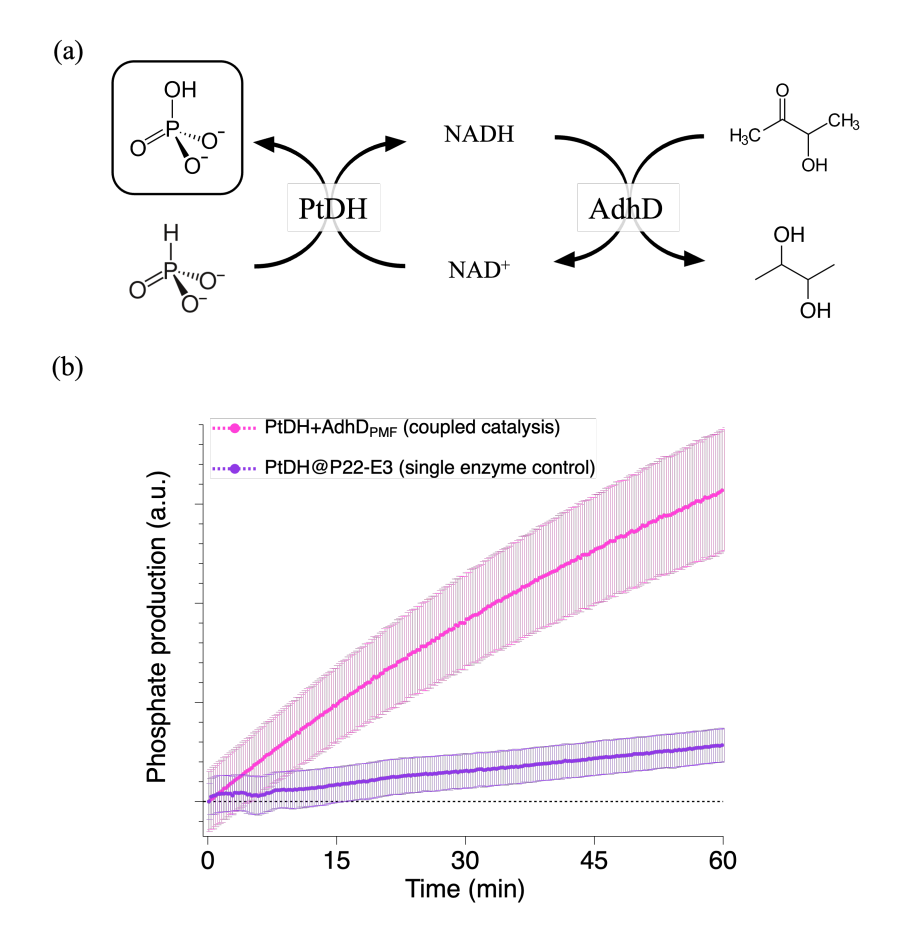


**Figure 4.** Multi-enzyme catalysis in the PMF. (a) Catalytic scheme of the PtDH and AdhD coupled enzymes. AdhD catalyzes the reduction of acetoin using NADH as the reductant, recycling NADH back to NAD $^+$  for the phosphite oxidation catalyzed by PtDH. (b) Phosphate production was detected at 360 nm over time using a phosphate detection assay to monitor the multi-enzyme activity with unmodified NADH substrate at I = 41 mM, pH 7.2. Free particle control with PtDH enzymes (single enzyme reaction) exhibited a slower production of phosphate over time, in contrast to the two-enzyme PMF reaction, likely due to the presence of NAD $^+$  in the substrate and the NADH auto-oxidation over time. The measured absorbance values were normalized by correction from absorbance at time zero and the rate of a mock reaction, to obtain the difference in absorbance over time to express the phosphate production as arbitrary units. All data points are expressed as mean  $\pm$  1 SD (n=3).

#### **CONCLUSIONS**

The higher-order PMF assembled via coiled-coil motifs on VLP surfaces offers a robust platform with the potential to construct versatile, functional materials that can accommodate, and are compatible with, mesophilic and somewhat fragile enzymes. We have shown that ordered packing of the particles in the material is not required for catalytic activity. The amorphous coiled-coil based PMF was constructed in a one-pot fabrication process resulting in a material that was stable across a wide range of ionic strength conditions, whose structure was not affected by the ionic strength modulations (unlike the free particle modular units). Although not to the same extent, both positively and negatively charged macromolecules partitioned into the highly charged PMF. Thus, the kinetic behavior we observed mirrors the charged substrate partitioning trends with only slight selectivity and enhancement of positively charged substrates, suggesting the potential of controlling the PMF kinetics by controlling the partitioning of substrates. Furthermore, because of the two-component nature of the VLP-VLP assembly, this material lends itself to incorporation of multiple enzymes in different types of particles for complex multi-step catalysis. To obtain a catalytic advantage with the constructed PMF compared to its free particle building block units, some factors could be strategically modified, including the choice of the encapsulated enzymes, the coiled-coil linker length (number of heptad repeats) to modulate the interstitial porosity, the charge and size of the substrates, and the ionic strength of the medium to modulate the extent of partitioning and mobility of the substrates.

### ASSOCIATED CONTENT

**Supporting information**. Protein sequences used in the study, additional experimental details, characterization data of P22 VLPs, SAXS analyses of the PMF and individual particle controls,

DLS and zeta potential data of proteins and modified substrates, dendrimer partitioning data, kinetic data of PtDH with modified and unmodified substrates, supplementary discussion sections.

#### **AUTHOR INFORMATION**

# **Corresponding Author**

\*Trevor Douglas

Department of Chemistry, Indiana University, Bloomington 47405, IN, United States; orcid.org/0000-0002-7882-2704; Email: <a href="mailto:trevdoug@indiana.edu">trevdoug@indiana.edu</a>

### **Author Contributions**

The manuscript was written through contributions of all authors. All authors have given approval to the final version of the manuscript.

#### **Notes**

The authors declare no competing financial interest.

# ACKNOWLEDGMENT

This work was supported by grants from the National Science Foundation (CMMI-1922883) and the Human Frontier Science Program (HFSPO RGP0012/2018). The authors thank the Laboratory for Biological Mass Spectrometry, Electron microscopy center, Light Microscopy Imaging Center (LMIC), Nanoscale Characterization Facility at Indiana University for access to their instruments. The OMX-SR microscope at the LMIC was acquired under the National Institutes of Health (NIH) award NIH1S10OD024988-01. This research used resources of the Advanced Photon Source, a U.S. Department of Energy (DOE) Office of Science user facility at

Argonne National Laboratory and is based on research supported by the U.S. DOE Office of

Science-Basic Energy Sciences, under Contract No. DE-AC02-06CH11357.

#### REFERENCES

- 1. Klem, M. T.; Young, M.; Douglas, T., Biomimetic synthesis of photoactive  $\alpha$ -Fe<sub>2</sub>O<sub>3</sub> templated by the hyperthermophilic ferritin from Pyrococus furiosus. *J. Mater. Chem.* **2010**, *20* (1), 65-67.
- 2. Wiedenheft, B.; Flenniken, M. L.; Allen, M. A.; Young, M.; Douglas, T., Bioprospecting in high temperature environments; application of thermostable protein cages. *Soft Matter* **2007**, *3* (9), 1091-1098.
- 3. Schultz, P., The interplay between chemistry and biology in the design of enzymatic catalysts. *Science* **1988**, *240* (4851), 426-433.
- 4. Zaera, F., The new materials science of catalysis: Toward controlling selectivity by designing the structure of the active site. *J. Phys. Chem. Lett.* **2010**, *1* (3), 621-627.
- 5. O'Neil, A.; Prevelige, P. E.; Douglas, T., Stabilizing viral nano-reactors for nerve-agent degradation. *Biomater. Sci.* **2013**, *1* (8), 881-886.
- 6. Wang, Y.; Uchida, M.; Waghwani, H. K.; Douglas, T., Synthetic virus-like particles for glutathione biosynthesis. *ACS Synth. Biol.* **2020**, *9* (12), 3298-3310.
- 7. Das, S.; Zhao, L.; Elofson, K.; Finn, M., Enzyme stabilization by virus-like particles. *Biochemistry* **2020**, *59* (31), 2870-2881.
- 8. Patterson, D. P.; LaFrance, B.; Douglas, T., Rescuing recombinant proteins by sequestration into the P22 VLP. *Chem. Commun.* **2013**, *49* (88), 10412-10414.
- 9. Fiedler, J. D.; Brown, S. D.; Lau, J. L.; Finn, M., RNA-directed packaging of enzymes within virus-like particles. *Angew. Chem., Int. Ed.* **2010**, *49* (50), 9648-9651.
- 10. Jordan, P. C.; Patterson, D. P.; Saboda, K. N.; Edwards, E. J.; Miettinen, H. M.; Basu, G.; Thielges, M. C.; Douglas, T., Self-assembling biomolecular catalysts for hydrogen production. *Nat. Chem.* **2016**, *8* (2), 179-185.
- 11. McCoy, K.; Uchida, M.; Lee, B.; Douglas, T., Templated assembly of a functional ordered protein macromolecular framework from P22 virus-like particles. *ACS Nano* **2018**, *12* (4), 3541-3550.
- 12. Selivanovitch, E.; Uchida, M.; Lee, B.; Douglas, T., Substrate Partitioning into Protein Macromolecular Frameworks for Enhanced Catalytic Turnover. *ACS Nano* **2021**, *15* (10), 15687-15699.
- 13. Aumiller, W. M.; Uchida, M.; Douglas, T., Protein cage assembly across multiple length scales. *Chem. Soc. Rev.* **2018**, *47* (10), 3433-3469.
- 14. Douglas, T.; Young, M., Viruses: making friends with old foes. *Science* **2006**, *312* (5775), 873-875.
- 15. Kraj, P.; Hewagama, N. D.; Douglas, T., Diffusion and molecular partitioning in hierarchically complex virus-like particles. *Virology* **2023**, *580*, 50-60.

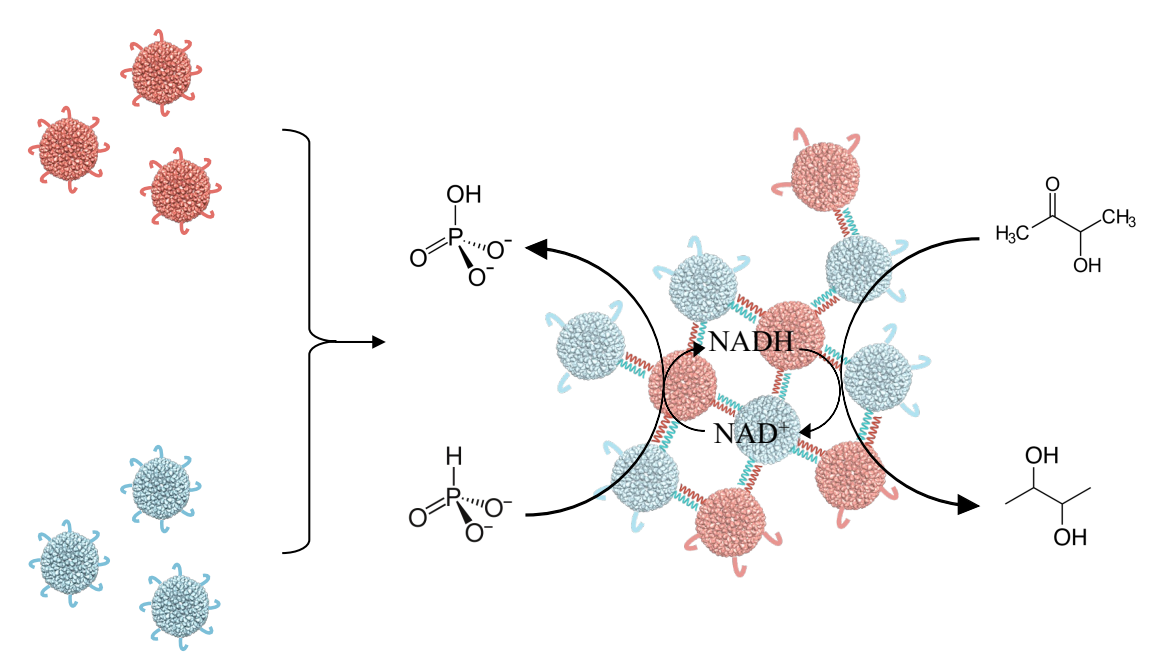
- 16. Uchida, M.; LaFrance, B.; Broomell, C. C.; Prevelige Jr, P. E.; Douglas, T., Higher Order Assembly of Virus-like Particles (VLPs) Mediated by Multi-valent Protein Linkers. *Small* **2015**, *11* (13), 1562-1570.
- 17. Uchida, M.; Klem, M. T.; Allen, M.; Suci, P.; Flenniken, M.; Gillitzer, E.; Varpness, Z.; Liepold, L. O.; Young, M.; Douglas, T., Biological containers: protein cages as multifunctional nanoplatforms. *Adv. Mater.* **2007**, *19* (8), 1025-1042.
- 18. Korpi, A.; Anaya-Plaza, E.; Välimäki, S.; Kostiainen, M., Highly ordered protein cage assemblies: A toolkit for new materials. *Wiley Interdiscip. Rev.: Nanomed. Nanobiotechnol.* **2020**, *12* (1), e1578.
- 19. Aumiller Jr, W. M.; Uchida, M.; Biner, D. W.; Miettinen, H. M.; Lee, B.; Douglas, T., Stimuli responsive hierarchical assembly of P22 virus-like particles. *Chem. Mater.* **2018**, *30* (7), 2262-2273.
- 20. Uchida, M.; Brunk, N. E.; Hewagama, N. D.; Lee, B.; Prevelige Jr, P. E.; Jadhao, V.; Douglas, T., Multilayered Ordered Protein Arrays Self-Assembled from a Mixed Population of Virus-like Particles. *ACS Nano* **2022**, *16* (5), 7662-7673.
- 21. Selivanovitch, E.; Douglas, T., Virus capsid assembly across different length scales inspire the development of virus-based biomaterials. *Curr. Opin. Virol.* **2019**, *36*, 38-46.
- 22. Botstein, D.; Waddell, C. H.; King, J., Mechanism of head assembly and DNA encapsulation in Salmonella phage P22: I. Genes, proteins, structures and DNA maturation. *J. Mol. Biol.* **1973**, *80* (4), 669-695.
- 23. O'Neil, A.; Reichhardt, C.; Johnson, B.; Prevelige, P. E.; Douglas, T., Genetically programmed in vivo packaging of protein cargo and its controlled release from bacteriophage P22. *Angew. Chem., Int. Ed.* **2011**, *50* (32), 7425-7428.
- 24. O'Neil, A.; Prevelige, P. E.; Basu, G.; Douglas, T., Coconfinement of fluorescent proteins: spatially enforced communication of GFP and mCherry encapsulated within the P22 capsid. *Biomacromolecules* **2012**, *13* (12), 3902-3907.
- 25. Patterson, D. P.; Prevelige, P. E.; Douglas, T., Nanoreactors by programmed enzyme encapsulation inside the capsid of the bacteriophage P22. *ACS Nano* **2012**, *6* (6), 5000-5009.
- 26. Patterson, D. P.; Schwarz, B.; Waters, R. S.; Gedeon, T.; Douglas, T., Encapsulation of an enzyme cascade within the bacteriophage P22 virus-like particle. *ACS Chem. Biol.* **2014**, *9* (2), 359-365.
- 27. Qazi, S.; Miettinen, H. M.; Wilkinson, R. A.; McCoy, K.; Douglas, T.; Wiedenheft, B., Programmed self-assembly of an active P22-Cas9 nanocarrier system. *Mol. Pharmaceutics* **2016**, *13* (3), 1191-1196.
- 28. Parent, K. N.; Khayat, R.; Tu, L. H.; Suhanovsky, M. M.; Cortines, J. R.; Teschke, C. M.; Johnson, J. E.; Baker, T. S., P22 coat protein structures reveal a novel mechanism for capsid maturation: stability without auxiliary proteins or chemical crosslinks. *Structure* **2010**, *18* (3), 390-401.
- 29. Teschke, C. M.; McGough, A.; Thuman-Commike, P. A., Penton release from P22 heat-expanded capsids suggests importance of stabilizing penton-hexon interactions during capsid maturation. *Biophys. J.* **2003**, *84* (4), 2585-2592.
- 30. Selivanovitch, E.; Koliyatt, R.; Douglas, T., Chemically induced morphogenesis of P22 virus-like particles by the surfactant sodium dodecyl sulfate. *Biomacromolecules* **2018**, *20* (1), 389-400.

- 31. Brunk, N. E.; Uchida, M.; Lee, B.; Fukuto, M.; Yang, L.; Douglas, T.; Jadhao, V., Linker-mediated assembly of virus-like particles into ordered arrays via electrostatic control. *ACS Appl. Bio Mater.* **2019**, *2* (5), 2192-2201.
- 32. Uchida, M.; McCoy, K.; Fukuto, M.; Yang, L.; Yoshimura, H.; Miettinen, H. M.; LaFrance, B.; Patterson, D. P.; Schwarz, B.; Karty, J. A., Modular self-assembly of protein cage lattices for multistep catalysis. *ACS Nano* **2018**, *12* (2), 942-953.
- 33. Servid, A.; Jordan, P.; O'Neil, A.; Prevelige, P.; Douglas, T., Location of the bacteriophage P22 coat protein C-terminus provides opportunities for the design of capsid-based materials. *Biomacromolecules* **2013**, *14* (9), 2989-2995.
- 34. Apostolovic, B.; Danial, M.; Klok, H.-A., Coiled coils: attractive protein folding motifs for the fabrication of self-assembled, responsive and bioactive materials. *Chem. Soc. Rev.* **2010**, *39* (9), 3541-3575.
- 35. Cristie-David, A. S.; Chen, J.; Nowak, D. B.; Bondy, A. L.; Sun, K.; Park, S. I.; Banaszak Holl, M. M.; Su, M.; Marsh, E. N. G., Coiled-coil-mediated assembly of an icosahedral protein cage with extremely high thermal and chemical stability. *J. Am. Chem. Soc.* **2019**, *141* (23), 9207-9216.
- 36. Fletcher, J. M.; Harniman, R. L.; Barnes, F. R.; Boyle, A. L.; Collins, A.; Mantell, J.; Sharp, T. H.; Antognozzi, M.; Booth, P. J.; Linden, N., Self-assembling cages from coiled-coil peptide modules. *Science* **2013**, *340* (6132), 595-599.
- 37. Stevens, M. M.; Flynn, N. T.; Wang, C.; Tirrell, D. A.; Langer, R., Coiled-coil peptide-based assembly of gold nanoparticles. *Adv. Mater.* **2004**, *16* (11), 915-918.
- 38. Minten, I. J.; Hendriks, L. J.; Nolte, R. J.; Cornelissen, J. J., Controlled encapsulation of multiple proteins in virus capsids. *J. Am. Chem. Soc.* **2009**, *131* (49), 17771-17773.
- 39. Minten, I. J.; Nolte, R. J.; Cornelissen, J. J., Complex assembly behavior during the encapsulation of green fluorescent protein analogs in virus derived protein capsules. *Macromol. Biosci.* **2010**, *10* (5), 539-545.
- 40. Pechar, M.; Pola, R.; Laga, R.; Ulbrich, K.; Bednárová, L.; Maloň, P.; Sieglová, I.; Král, V.; Fábry, M.; Vaněk, O. e., Coiled coil peptides as universal linkers for the attachment of recombinant proteins to polymer therapeutics. *Biomacromolecules* **2011**, *12* (10), 3645-3655.
- 41. Kopeček, J.; Yang, J., Smart self-assembled hybrid hydrogel biomaterials. *Angew. Chem., Int. Ed.* **2012,** *51* (30), 7396-7417.
- 42. Utterström, J.; Naeimipour, S.; Selegård, R.; Aili, D., Coiled coil-based therapeutics and drug delivery systems. *Adv. Drug Delivery Rev.* **2021**, *170*, 26-43.
- 43. Chao, H.; Bautista, D. L.; Litowski, J.; Irvin, R. T.; Hodges, R. S., Use of a heterodimeric coiled-coil system for biosensor application and affinity purification. *J. Chromatogr. B: Biomed. Sci. Appl.* **1998**, *715* (1), 307-329.
- 44. Wang, Y.; Selivanovitch, E.; Douglas, T., Enhancing Multistep Reactions: Biomimetic Design of Substrate Channeling Using P22 Virus-Like Particles. *Adv. Sci.* **2023**, *10* (13), 2206906.
- 45. Fairman, R.; Chao, H. G.; Mueller, L.; Lavoie, T. B.; Shen, L.; Novotny, J.; Matsueda, G. R., Characterization of a new four-chain coiled-coil: Influence of chain length on stability. *Protein Sci.* **1995**, *4* (8), 1457-1469.
- 46. Su, J. Y.; Hodges, R. S.; Kay, C. M., Effect of chain length on the formation and stability of synthetic. alpha.-helical coiled coils. *Biochemistry* **1994**, *33* (51), 15501-15510.

- 47. Selivanovitch, E.; LaFrance, B.; Douglas, T., Molecular exclusion limits for diffusion across a porous capsid. *Nat. Commun.* **2021**, *12* (1), 2903.
- 48. Hung, J. E.; Fogle, E. J.; Christman, H. D.; Johannes, T. W.; Zhao, H.; Metcalf, W. W.; Van Der Donk, W. A., Investigation of the Role of Arg301 Identified in the X-ray Structure of Phosphite Dehydrogenase. *Biochemistry* **2012**, *51* (21), 4254-4262.
- 49. Zou, Y.; Zhang, H.; Brunzelle, J. S.; Johannes, T. W.; Woodyer, R.; Hung, J. E.; Nair, N.; Van Der Donk, W. A.; Zhao, H.; Nair, S. K., Crystal structures of phosphite dehydrogenase provide insights into nicotinamide cofactor regeneration. *Biochemistry* **2012**, *51* (21), 4263-4270.
- 50. Lindhout, D. A.; Litowski, J. R.; Mercier, P.; Hodges, R. S.; Sykes, B. D., NMR solution structure of a highly stable de novo heterodimeric coiled-coil. *Biopolymers* **2004**, *75* (5), 367-375.
- 51. Machielsen, R.; Uria, A. R.; Kengen, S. W.; van der Oost, J., Production and characterization of a thermostable alcohol dehydrogenase that belongs to the aldo-keto reductase superfamily. *Appl. Environ. Microbiol.* **2006**, *72* (1), 233-238.

# GRAPHIC FOR MANUSCRIPT

# TABLE OF CONTENTS (TOC) GRAPHIC



VLPs encapsulated with enzymes

PMF assembled via heterodimeric coiled-coil interactions